PHYSICAL REVIEW B **89**, 214117 (2014)

Phase field crystal modeling as a unified atomistic approach to defect dynamics

Joel Berry,[1,2,*] Nikolas Provatas,[3] Jörg Rottler,[2] and Chad W. Sinclair[4]
[1]*Department of Materials Science and Engineering, McMaster University, 1280 Main Street West, Hamilton, Ontario, Canada L8S 4L7*
[2]*Department of Physics and Astronomy, The University of British Columbia, 6224 Agricultural Road, Vancouver, British Columbia, Canada V6T 1Z1*
[3]*Physics Department, McGill University, 3600 rue University, Montréal, Québec, Canada H3A 2T8*
[4]*Department of Materials Engineering, The University of British Columbia, 309-6350 Stores Road, Vancouver, British Columbia, Canada V6T 1Z4*

(Received 2 December 2013; revised manuscript received 4 June 2014; published 30 June 2014)

Material properties controlled by evolving defect structures, such as mechanical response, often involve processes spanning many length and time scales which can not be modeled using a single approach. We present a variety of results that demonstrate the ability of phase field crystal (PFC) models to describe complex defect evolution phenomena on atomistic length scales and over long, diffusive time scales. Primary emphasis is given to the unification of conservative and nonconservative dislocation creation mechanisms in three-dimensional fcc and bcc materials. These include Frank-Read–type glide mechanisms involving closed dislocation loops or grain boundaries as well as Bardeen-Herring–type climb mechanisms involving precipitates, inclusions, and/or voids. Both source classes are naturally and simultaneously captured at the atomistic level by PFC descriptions, with arbitrarily complex defect configurations, types, and environments. An unexpected dipole-to-quadrupole source transformation is identified, as well as various complex geometrical features of loop nucleation via climb from spherical particles. Results for the strain required to nucleate a dislocation loop from such a particle are in agreement with analytic continuum theories. Other basic features of fcc and bcc dislocation structure and dynamics are also outlined, and initial results for dislocation-stacking fault tetrahedron interactions are presented. These findings together highlight various capabilities of the PFC approach as a coarse-grained atomistic tool for the study of three-dimensional crystal plasticity.

DOI: 10.1103/PhysRevB.89.214117 PACS number(s): 61.72.Bb, 61.72.Lk, 62.20.F−, 81.40.Lm

I. INTRODUCTION

The macroscopic mechanical properties of crystals and polycrystals are primarily consequences of complex collective interactions between atomic level defects. The characteristic scales of these interaction processes can span many orders of magnitude in length and time, presenting major fundamental challenges to the development of a unified modeling approach. In particular, line defects or dislocations, which are the central mediators of plasticity in many systems, can evolve rapidly via conservative mechanisms (e.g., glide and cross slip) or relatively slowly via nonconservative mechanisms mediated by interactions with point defects (e.g., climb). Characteristic length scales of dislocation structures range from atomic dimensions to micron level and up for collective, organized arrays. A complete model of dislocation dynamics would therefore ideally include the fundamental physics of dislocation creation, interaction, annihilation/absorption, etc., via both conservative and nonconservative mechanisms, accessible across all relevant length and time scales. This is not feasible with any presently available model. Other classes of defects (point, planar, and bulk) should also be considered in a more general model of crystalline materials subjected to driving forces.

Elements of conservative dislocation processes are often quite readily modeled at the atomic level using approaches such as molecular dynamics (MD) [1,2]. These conservative mechanisms have also been built into larger length-scale mesoscopic modeling approaches such as discrete dislocation dynamics (DDD) [1,3,4] and continuum phase field (PF) dislocation models [1,5,6]. Basic conservative processes are generally implemented in DDD with detailed rule-based formulations that consider some number of the innumerable possible defect interaction scenarios. PF models avoid this complexity by treating select dislocation lines as interfaces in a continuum field description. These interfaces interact and evolve automatically in response to local driving forces. The cost is greater computational demand since the PF equations must be solved throughout the entire system, not only at localized dislocation positions.

Nonconservative dislocation processes present another set of challenges to plasticity models, as these motions are mediated by vacancy diffusion and are therefore inherently difficult to access on conventional atomistic simulation time scales. Climb becomes relevant and often dominant at high temperatures or large vacancy concentrations, and is fundamental to such phenomena as creep, annealing, recrystallization, and irradiation damage. Elements of climb have been built into DDD [7–10] and PF [11,12] models, although this issue is still in many ways under development. Meaningful coarse-grained input parameters and their values, for example, which would ideally be extracted from microscopic simulations, are lacking.

No atomistic modeling approach has yet proven capable of consistently describing both conservative and nonconservative dislocation processes over both nanoscales and mesoscales. In this work, we present results for a method that unifies both types of dislocation motion on atomistic length scales. Phase field crystal (PFC) models [13–15] describe diffusive

---

[*] Current address: Department of Mechanical and Aerospace Engineering, Princeton University, Princeton, NJ 08544; jmberry@princeton.edu

dynamics in condensed matter systems with atomistic resolution, and are therefore potentially capable of bridging the gap between fast glide plasticity and slow climb plasticity at the nanoscale. Defect superstructures of arbitrary complexity can be studied, including polycrystals with nearly any variation/combination of dislocation, grain boundary, precipitate, and stacking fault configurations, for example. The ability to naturally describe arbitrary defect structures is a feature of atomistic approaches that is inherently absent from mesoscale approaches. The larger length scales described by DDD and PF models can not currently be reached by PFC, although one may imagine using PFC simulations to generate input parameters for such models or numerically coupling PFC with DDD or PF. Coarse-grained complex amplitude PFC models also provide an interesting means of self-consistently reaching larger length scales [16–21].

The goals of this work are to demonstrate that simple PFC models naturally capture well-established conservative dislocation creation mechanisms as well as central elements of the relatively poorly understood nonconservative dislocation creation mechanisms, which can not be easily studied with other methods. These goals are part of a larger effort to exploit the novel features of the PFC approach within traditional areas of materials science, including crystal plasticity, structural phase transformations, and microstructure evolution [21–26]. Some initial groundwork covering fundamental dislocation properties in fcc materials was reported by the present authors in Ref. [25]. Perfect dislocations and simple grain boundaries in two-dimensional (2D) triangular and three-dimensional (3D) bcc crystals have also been examined in various contexts [14,15,27–38].

The rest of this paper is organized as follows. In Sec. II, the basic model equations, numerical solution methods, and strain application procedures are outlined. In Sec. III, some qualitative and quantitative features of the specific dislocations relevant to fcc and bcc plasticity are surveyed in the PFC framework. In Sec. IV, conservative Frank-Read–type dislocation sources in fcc materials are studied in two contexts. The first considers controlled nucleation of dislocation loop dipoles, and an alternate mechanism whereby a dipole source transforms into a quadrupole source is reported. The second context considers uncontrolled nucleation of partial and perfect dislocations from grain boundaries in nanopolycrystalline samples. In Sec. V, nonconservative Bardeen-Herring–type dislocation sources in bcc materials are studied. The case of uniform loop nucleation from spherical inclusions or precipitates is considered. A range of complex nucleation behaviors caused by nontrivial interactions between interface structure, strain orientation, and dislocation energetics are examined. Selected results are compared with earlier analytic predictions and shown to agree well when the analytic theories are adapted to the scenario considered in our simulations. Finally, a brief presentation of stacking fault tetrahedron (SFT) formation and SFT-dislocation interactions is provided in Sec. VI.

II. MODEL AND METHODS

The standard PFC free-energy functional, modified to stabilize fcc stacking faults as described in Ref. [25], is used for all fcc systems studied in the following sections. It is written as

$$\tilde{F} = \int d\vec{r}\left[\frac{1}{2}n^2(\vec{r}) - \frac{w}{6}n^3(\vec{r}) + \frac{u}{12}n^4(\vec{r})\right] - \frac{1}{2}\iint d\vec{r}\, d\vec{r}_2 n(\vec{r}) C_2(|\vec{r}-\vec{r}_2|) n(\vec{r}_2), \tag{1}$$

where $\tilde{F} = F/(k_B T \rho_\ell)$, ρ_ℓ is a constant reference density, $n(\vec{r}) = \rho(\vec{r})/\rho_\ell - 1$ is the rescaled atomic density field, $\rho(\vec{r})$ is the unscaled atomic number density field, w and u are coefficients treated as free parameters to provide additional model flexibility, and $C_2(|\vec{r}-\vec{r}_2|)$ is the two-point direct correlation function of the fluid, assumed isotropic. The modified standard PFC kernel [which approximates the full $C_2(|\vec{r}-\vec{r}_2|)$] after Fourier transformation reads as

$$\hat{C}_2(k) = -r + 1 - B^x(1-\tilde{k}^2)^2 - H_0 e^{-(k-k_0)^2/(2\alpha_0^2)}, \tag{2}$$

where r is a constant proportional to temperature, B^x is a constant proportional to the solid-phase elastic moduli, $\tilde{k} = k/(2\pi)$ is the normalized wave number, H_0 is a constant related to stacking fault energy γ_{ISF}, $k_0 = 2\pi\sqrt{41/12}/a$, a is the equilibrium lattice constant, and α_0 is an additional constant related to γ_{ISF}. $n(\vec{r})$ will be allowed to assume nonzero average values n_0, and it will be implied that $w = 0$ and $u = 3$ for all fcc simulations.

The structural or XPFC free-energy functional class [22–24] is used for all bcc systems studied in the following sections. It is written as Eq. (1) with the Fourier transformed kernel

$$\hat{C}_2(k)_i = e^{-(k-k_i)^2/(2\alpha_i^2)} e^{-\sigma^2 k_i^2/(2\rho_i\beta_i)}, \tag{3}$$

where i denotes a family of lattice planes at wave number k_i, and σ is a temperature parameter. The constants α_i, ρ_i, and β_i are the Gaussian width (which sets the elastic constants), planar atomic density, and number of planes, respectively, associated with the ith family of lattice planes. The envelope of all selected Gaussians i composes the final $\hat{C}_2(k)$. Only one reflection at $k_1 = 2\sqrt{2}\pi/a$ where $a = \sqrt{2/3}$ will be used here, as this is all that is necessary to produce equilibrium bcc structures.

Two dynamic equations for $n(\vec{r})$ will be considered. The first is a purely diffusive Model B form

$$\frac{\partial n(\vec{r})}{\partial t} = \nabla^2 \frac{\delta \tilde{F}}{\delta n(\vec{r})}, \tag{4}$$

where t is dimensionless time. The second equation of motion introduces a faster inertial, quasiphonon dynamic component in addition to diffusive dynamics [28]

$$\frac{\partial^2 n(\vec{r})}{\partial t^2} + \beta \frac{\partial n(\vec{r})}{\partial t} = \alpha^2 \nabla^2 \frac{\delta \tilde{F}}{\delta n(\vec{r})}, \tag{5}$$

where α and β are constants related to sound speed and damping rate, respectively. All simulations were performed in 3D using a pseudospectral algorithm with semi-implicit time stepping and periodic boundary conditions. Deformation was applied via strain-controlled methods for both simple shear and uniaxial tension or compression simulations. Constant strain rates were employed for both deformation types.

III. SOME FUNDAMENTAL ELEMENTS OF fcc AND bcc CRYSTAL PLASTICITY

Many aspects of the distinct plastic response of fcc and bcc crystals can be understood in terms of structural and dynamic differences between the dominant carriers of plasticity in either lattice. The primary dislocation type in fcc materials is that with total Burgers vector $a/2\langle 110\rangle$, dissociated into two $a/6\langle 112\rangle$ Shockley partials connected by a stacking fault. Such dissociated dislocations provide fcc crystals with 12 active primary slip systems, all of type $\{111\}\langle 110\rangle$. The very small Peierls stress of the Shockley partials can explain the low yield stress of fcc materials, and the subsequent formation of large numbers of dislocation junctions and stacking faults can explain their excellent work-hardening properties, ductility, and the commonly observed formation of mesoscale dislocation patterns [39].

The primary dislocation type in bcc materials is that with Burgers vector $a/2\langle 111\rangle$. This dislocation is glissile within 48 potential primary slip systems of type $\{110\}\langle 111\rangle$, $\{112\}\langle 111\rangle$, or $\{123\}\langle 111\rangle$. The nonplanar core structure of the $a/2\langle 111\rangle$ screw dislocation in particular at low temperatures leads to a much smaller glide mobility than that in edge orientation. The $a/2\langle 111\rangle$ screw dislocation therefore controls plastic flow in bcc crystals at $T \lesssim 0.15T_{\text{melt}}$. Its high Peierls stress can explain the large yield and flow stresses of bcc crystals, as well as the absence of mesoscale dislocation patterning at low to moderate stresses [39].

It can therefore be argued that these dislocation types must be stabilized and their basic core features reproduced if one wishes to perform atomistic PFC simulations of fcc and bcc plasticity. We have found that it is indeed possible to stabilize both of these dislocation types within a given PFC model. Dissociated $a/2\langle 110\rangle$ fcc dislocations were previously studied by the current authors [25]. With proper selection of the model parameters, static properties (dissociation width, Peierls strains, etc.) and glide dynamics of these dislocations were found to be in good agreement with other atomistic calculations and continuum elastic theories. For the primary bcc $a/2\langle 111\rangle$ screw dislocation, we have found that the PFC model used in this study reproduces the same nondegenerate nonpolarized core configuration obtained from density functional theory calculations and MD simulations employing various empirical potentials [40] (see Fig. 1). The central core features of the primary dislocation types in both fcc and bcc crystals can therefore be well captured by PFC models. This level of accuracy in terms of core structure should not always be expected, especially for more complex, directionally bonded materials such as diamond cubic Si or Ge crystals. Nonetheless, when sufficient accuracy is achieved, we find as a general consequence that the correct slip systems naturally emerge during simulations of plastic flow, and that atomistically detailed plasticity mechanisms also often follow.

For example, we have confirmed that the glide mobility of the bcc $a/2\langle 111\rangle$ dislocation in screw orientation is significantly lower than that in edge orientation, as expected based on the nonplanar screw core structure. This mobility difference was inferred from zero-strain simulations of glide-mediated dipole annihilation, in which it was observed that screw dislocation dipoles take roughly one to two orders of magnitude longer to annihilate than edge dipoles at equal initial separations.

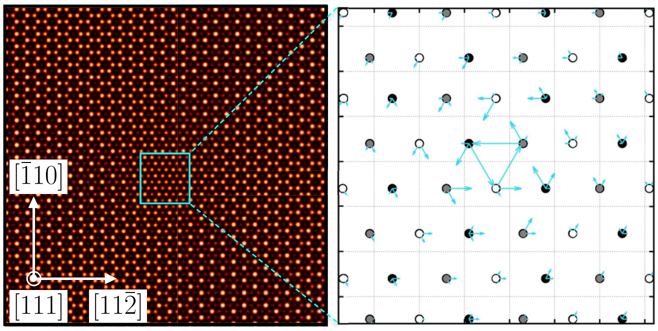

FIG. 1. (Color online) The bcc $a/2\langle 111\rangle$ screw dislocation from a single-peaked XPFC model. A cross section of $n(\vec{r})$ is shown on the left, and the differential displacement map [41] around the core is shown on the right. Results were generated using Eqs. (1), (3), and (4) with model parameters $w = 1.4$, $u = 1$, $n_0 = 0.05$, $\alpha_1 = 0.25$, $\sigma = 0.12$, $\rho_1 = 1$, and $\beta_1 = 8$. Nearly identical results are obtained at $\alpha_1 = 1$ and 2.

These same basic structural and energetic features also influence climb processes. For example, compressive and tensile strains along the axis of the dislocation Burgers vector induce the correct positive and negative climb directions in PFC simulations. Jogged dislocations subjected to the same type of strain climb in the expected fashion in which jogs diffusively translate along the line direction. The result is a net motion in the climb direction perpendicular to the glide plane (see Supplemental Material [42] for animations). If no jogs are present, climb proceeds by a more uniform simultaneous translation of larger line segments or of the entire line, although the energy barrier for this type of climb is larger than that of diffusive jog translation.

As shown previously for 2D triangular crystals in PFC [27,28], we find in 3D that uniform climb velocities of undissociated dislocations in the limit of low dislocation density ($\rho_d \lesssim 10^{13}$ m^{-2}) follow a power law as a function of applied stress, $v \sim \sigma^m$, with $m \sim 1$ for both dynamic equations (4) and (5). Apparent exponents m as large as 4 can appear at higher dislocation densities. Qualitatively similar behaviors as a function of ρ_d have been observed in kinetic Monte Carlo simulations [43].

We also note that screw dislocation cross slip readily occurs in 3D PFC simulations, and we find that the cross-slip barrier for dissociated fcc screw dislocations increases strongly with dissociation width and therefore with inverse stacking fault energy (see Supplemental Material [42] for animations). Such results, although far from a complete survey, demonstrate that relatively simple PFC models are capable of capturing many of the central atomistic features of plasticity in fcc and bcc materials over diffusive time scales.

IV. FRANK-READ–TYPE GLIDE SOURCES

The Frank-Read dislocation multiplication mechanism is an important element of crystal plasticity that has been widely observed and studied both experimentally and via computer simulations [44–47]. In the most commonly discussed scenario, a dislocation line pinned at two points within its glide plane bows out under stress until it meets itself on the opposite side of the pinning points. The contacting segments annihilate, resulting in a single loop and the original pinned segment, which then repeats the process if sufficient strain energy is still available. The many possible manifestations of this basic mechanism, including pinning of existing dislocation lines and emission of new line segments from grain boundaries (which act as pinning centers), contribute centrally to the large increases in dislocation density that occur during plastic deformation.

Although Frank-Read mechanisms occur via conservative dislocation motion and are therefore readily studied with conventional MD [44] and/or mesoscale continuum methods [46,47], we consider them here because of their general importance in plastic deformation processes, to demonstrate that the basic physics of such sources is well captured by PFC models. Nonconservative dislocation creation methods are separately considered in the following section. Unless noted otherwise, all simulations presented in this section describe fcc materials and employ Eqs. (1), (2), and (5).

A. Prismatic sources

We first examine a Frank-Read dipole source consisting of a single rectangular, prismatic edge dislocation loop in which the $a/2\langle 110\rangle$ lines along the $[1\bar{1}1]$ direction are relatively immobile (sessile), while the dissociated lines along the $[\bar{1}12]$ direction are mobile (glissile) [see Figs. 2 and 3(a)]. The $[1\bar{1}1]$ lines act as pinning points, such that under applied shear strain ϵ_{zy} the glissile lines bow out via glide in opposite directions. This setup was used in the MD simulations of Ref. [44]. Such a loop could in principle be formed, for example, by vacancy agglomeration following plastic deformation or irradiation, but it more generally provides a convenient source configuration that is entirely analogous to that of a longer jogged or locally pinned line segment.

To allow application of simple shear strain ϵ_{zy}, the standard penalty function approach was used [28]. The penalty function is written as an additional free-energy term of the form $M(\vec{r})[n(\vec{r})-n_p(\vec{r})]^2$, where $M(\vec{r})$ controls the strength of the penalty field and $n_p(\vec{r})$ is the configuration of the penalty field.

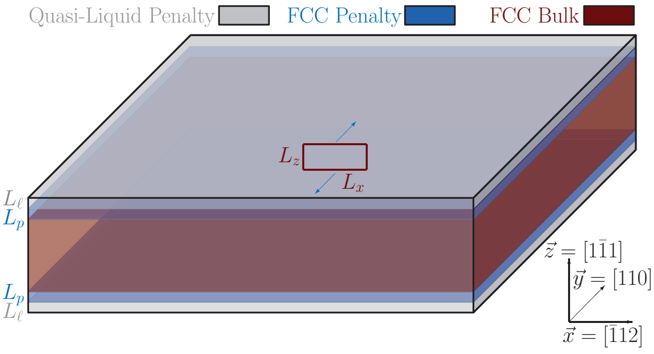

FIG. 2. (Color online) Schematic of the simulation setup used for Frank-Read source operation.

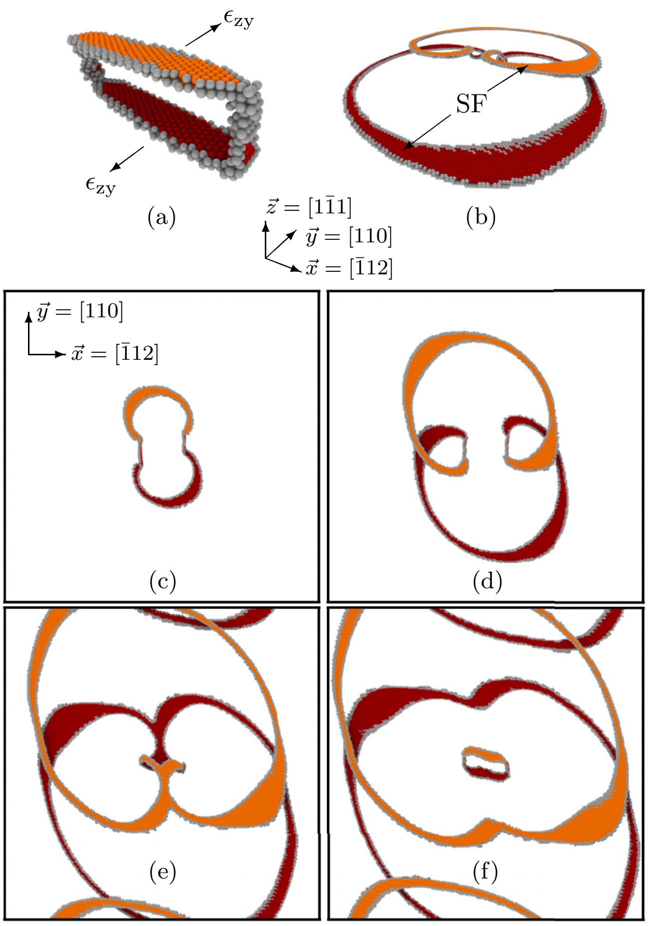

FIG. 3. (Color online) Operation of a Frank-Read dipole source under shear strain ϵ_{zy}. (a) A dislocation loop composed of four $a/2\langle 110\rangle$ edge dislocations. The two mobile horizontal segments are dissociated in the $(1\bar{1}1)$ plane, the two vertical segments are relatively immobile. (b) 3D view of the source near pinch off at $560t$. (c), (d), (e), and (f) show xy-plane views at $t=375$, 500, 595, and 625, respectively. For analysis and visualization purposes, local peaks in $n(\vec{r})$, which represent the most probable atomic positions, are taken to correspond to atomic sites. Density peaks with hcp coordination (stacking faults) are shown in orange (light) or red (dark) depending on position along the out-of-plane z axis. Those with irregular coordination (dislocation core) are shown in gray. See Supplemental Material [42] for the associated animation.

We specify

$$M(\vec{r}),n_p(\vec{r}) = \begin{cases} M_\ell, n_0 & \text{if} \quad z\in L_\ell,\\ M_P, n^{\text{EQ}}_{\text{fcc}}(\vec{r}) & \text{if} \quad z\in L_P,\\ 0,0 & \text{otherwise,}\end{cases} \tag{6}$$

where M_ℓ, M_P, L_ℓ, and L_P are constants (see Fig. 2) and $n^{\text{EQ}}_{\text{fcc}}(\vec{r})$ is the commensurate equilibrium fcc $n(\vec{r})$. The resulting system is a thin infinite slab of fcc bounded in the z direction by a homogeneous quasiliquid phase of width $2L_\ell$. The quasiliquid layer simply circumvents any unphysical strains that would otherwise be caused by the large shear disregistry at the periodic z boundary. Simple shear strain ϵ_{zy} can then be applied to the crystalline slab by translating the upper pinned region L_p along $+\vec{y}$ and the lower pinned region L_p along $-\vec{y}$ at some constant velocity. When Eq. (5) is employed to

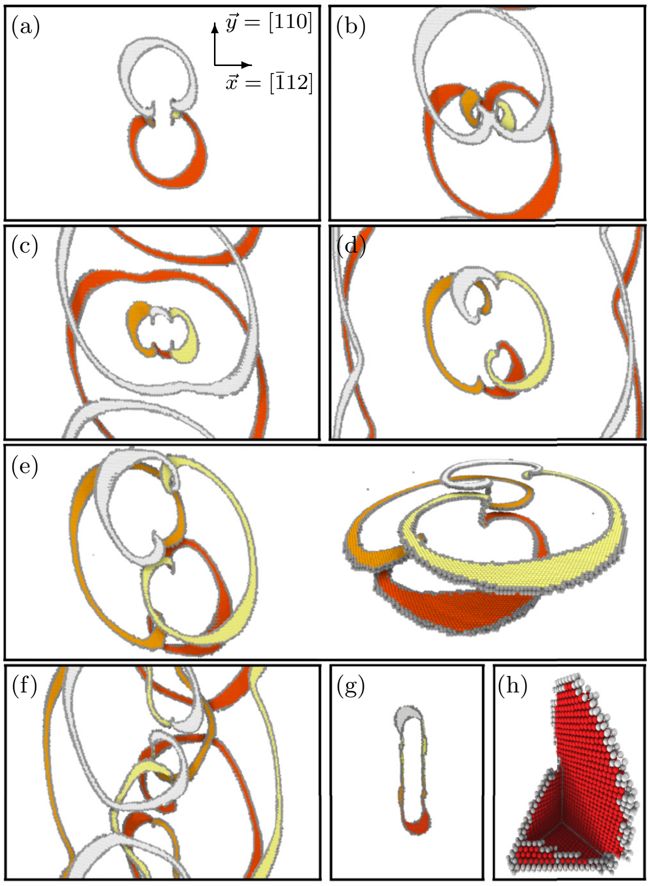

FIG. 4. (Color online) Operation of a Frank-Read dipole-to-quadrupole source. The initial loop is shorter in the x direction and longer in the z direction than that of Fig. 3. (a), (b), (c), (d), (e), (f), and (g) show xy-plane views at $t = 450, 520, 580, 680, 750, 840$, and 1030, respectively. A 3D view at $t = 750$ is also shown in (e). The source emits two initial loops near $520t$, then reorients and converts into a quadrupole source before being restored to a closed-loop form near $1030t$. Density peaks with hcp coordination (stacking faults) are shown in white, yellow (light gray), orange (gray), or red-orange (dark gray), depending on position along the out-of-plane z axis. Those with irregular coordination (dislocation cores) are shown in gray. (h) An unzipped stacking fault tetrahedron acting as a Frank-Read–type source. Density peaks with hcp coordination (stacking faults) are shown in red (dark gray), those with irregular coordination (dislocation cores) are shown in gray. See Supplemental Material [42] for the associated animations.

allow rapid elastic relaxations, a nearly uniform shear profile is produced across the sample.

Various initial loop sizes and stacking fault energies were considered, with two representative results shown in Figs. 3 and 4 (see Supplemental Material [42] for the associated animations). In both cases, model parameters $n_0 = -0.48$, $r = -0.63$, $B^x = 1$, $\alpha_0 = 1/2$, $k_0 = 6.2653$, $H_0 = 0.025$, $\beta = 0.01$, and $\alpha = 1$ were used. Additional simulation details are given here [48]. To estimate simulation time scales, we match the numerically measured fcc vacancy diffusion constant $D_v \simeq 1.0a^2/t$ to that of Cu at 1063 °C ($D_v \simeq 10^{-13}$ m^2/s, $a \simeq 0.36$ nm) [27]. The time unit t is then found to correspond to $\sim$1.3 μs, and the shear rate $0.000235/t$ converts to $\sim 180/s$, which is roughly five orders of magnitude lower than that of a typical and comparable MD simulation (applying 1.8% strain in 1 ns produces a rate of 1.8×10^7/s or see, e.g., Ref. [49]). Other fcc shear rates used in this study range from $\sim$10/s–800/s.

The operation of the dipole source shown in Fig. 3 closely follows the basic Frank-Read mechanism, with slight asymmetries in loop shape caused by image stresses in the z direction and interactions between opposing loops. Also, the $[1\bar{1}1]$ line segments, though sessile, do not respond purely rigidly to local stresses, they are not perfectly pinned to their initial lattice locations. As the shear strain ϵ_{zy} increases and the Frank-Read loops begin to bow out, the growing forces exerted on the $[1\bar{1}1]$ segments stretch these lines such that their angle from vertical θ becomes larger than that of the applied shear $\theta_A = \tan \epsilon_{zy}$. These small strain relief mechanisms also contribute to the asymmetric shape of the growing loops, and can lead to more complex effects when the prismatic loop dimensions and strain rate are varied.

One such effect is shown in Fig. 4. Here, the initial $[\bar{1}12]$ line segments are shorter and the initial $[1\bar{1}1]$ segments are longer. When the $[1\bar{1}1]$ segments stretch under the influence of the loop bow-out stresses, they begin to approach alignment with the nearest of the four $\{111\}$ planes. They are then able to lower their energy by taking a periodically jogged configuration with dissociated glissile segments in adjacent $\{111\}$ planes, each connected by a single jog where the lines are locally constricted. After the maximum bow-out stress has been overcome and the growing loops become nearly circular [Fig. 4(a)], the now jogged pinning lines begin to hinge back toward vertical. Rather than returning to their original undissociated, unjogged configuration, the most highly strained segments near the loop ends cross slip at their constricted jog sites onto the $(1\bar{1}1)$ glide plane normal to the z direction. These segments can not easily cross slip back to the original configuration, they instead begin to bow out on the $(1\bar{1}1)$ plane with the same jog sites now serving as pinning points for the new sources.

Depending on L_z and $\dot{\epsilon}_{zy}$, the number of new intermediate loops nucleated can vary. In the case of Fig. 4, two additional loops are formed and the dipole is converted into a quadrupole. The stresses exerted by the new loops cause the $[1\bar{1}1]$ lines to reorient such that all segment pairs align with the shear direction and the bow-out direction becomes perpendicular to the shear direction [Figs. 4(d) and 4(e)[. Once all four loops are pinched off, the initial loop configuration is restored [Fig. 4(g)].

If the maximum or activation stress of the initial source is low, then the $[1\bar{1}1]$ segments may never reach the angle required to attain a stepped configuration or may attain a stepped configuration with only very short glissile segments. In such a case, no additional sources are formed. As the maximum or activation stress of the initial source increases, the length of the resulting glissile segments in the stepped configuration also increases. If the length of any of these segments becomes large enough to activate its operation as a new source for a given stress, then it will bow out and begin forming a new loop. This type of transformation is therefore most likely to occur when such sources have a large activation stress, which for Frank-Read [45] sources $\sim 1/L_x$, corresponding to small L_x.

Greater potential segmentation lengths (large L_z) also favor this behavior. These expectations are in agreement with our results.

Such a transformation from dipole to multidipole also requires that the pinning points have some small, nonzero mobility, i.e., the pinning is not absolute. This condition is perhaps more applicable to soft crystalline materials such as colloidal crystals than to metals, for example, but similar imperfect pinning behaviors have been reported in MD and atomistic quasicontinuum studies of metallic crystals [50–52]. Such transformations may therefore be observable in MD simulations. Analogous situations should also become more probable, for example, following a rapid quench or at high temperatures where vacancy concentrations are large and climb is active.

The general behaviors discussed in these two examples exhibit some dependence on stacking fault energy $\gamma_{\rm ISF}$. When $\gamma_{\rm ISF}$ is small, the strain required to operate the source tends to be lowest, and the pinning segments remain relatively immobile throughout operation. When $\gamma_{\rm ISF}$ is large, the strain required to operate the source increases, and the forces exerted on the pinning segments by the bowing loops increase such that the pinning segments may be dragged through the crystal, effectively destroying the source.

It was also observed that stacking fault tetrahedra, created under low $\gamma_{\rm ISF}$ conditions, can act somewhat similarly as multipolar Frank-Read–type sources at high strains [42]. The $a/6\langle 011\rangle$ Lomer-Cottrell (LC) stair-rod junctions that make up the SFT edges are sessile, but under sufficient stress they may unzip and emit $a/6\langle 112\rangle$ Shockley partials that are pinned to neighboring vertices of the tetrahedron. The emitted segments bow out and can eventually form new, freely growing loops [see Fig. 4(h)]. The observed critical strain for unzipping and activation of the leading Shockley partial bow out ($\sim\mu/25$ where μ is the shear modulus) was found to decrease as either $\gamma_{\rm ISF}$ or the SFT size is increased.

B. Grain-boundary sources

Dislocations can also be emitted from or absorbed into grain boundaries during plastic deformation. The initiation of this type of nucleation process is more structurally complex than those already discussed due to the disordered nature of high-angle grain boundaries, but the basic elements of the Frank-Read mechanism are still present. If stress builds up near or within a grain boundary, it may be relieved by grain-boundary sliding or migration, for example, but in many cases strain is most readily relieved by spontaneously nucleating new dislocation lines which are then translated into the grain interior. These lines may begin as small half-loops pinned to the boundary at either end, which then bow out much like a Frank-Read source. Rather than sweeping around the pinning points and pinching off a complete loop (the grain boundary generally prevents this), the pinning points are more likely to migrate along the grain boundary as the half-loop grows.

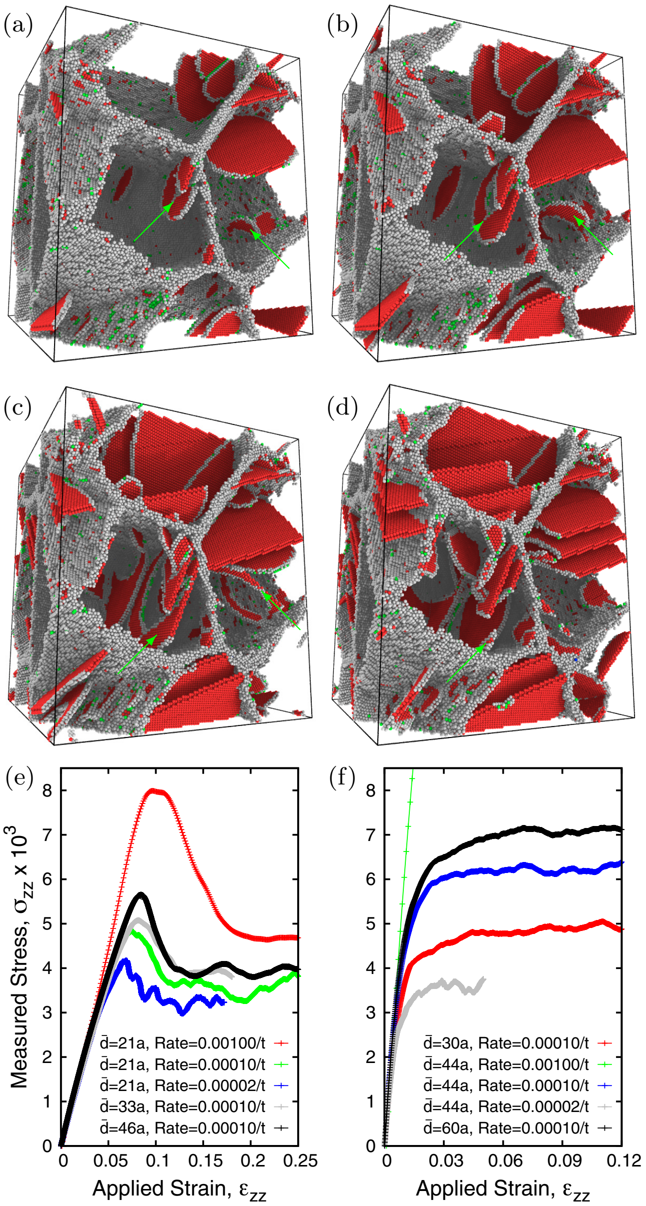

FIG. 5. (Color online) Emission of dissociated $a/2\langle 110\rangle$ dislocations and $a/6\langle 121\rangle$ partials from grain boundaries. (a)–(d) Nanopolycrystalline fcc sample with average grain size $\bar{d} \simeq 46a$ under tensile strain $\epsilon_{zz} = 0.082$, 0.086, 0.092, and 0.1, respectively. Both full dislocations [leading and trailing partials with stacking faults, two of which are tracked by green (light gray) arrows] and leading partials with stacking faults are emitted from or absorbed into grain boundaries, beginning near the yield point. Density peaks with hcp (stacking faults), irregular (dislocation cores), and fcc coordination are shown in red (dark gray), gray, and green (light gray), respectively. (e) Stress-strain curves for fcc polycrystals with various average grain sizes $\bar{d}$ and applied strain rates (constant strain rate tensile deformation). Model parameters are the same as those of Figs. 3 and 4. (f) As (e), but for bcc polycrystals with model parameters identical to those reported in Sec. V, except $\alpha_1 = 2$, and Eq. 5 was employed with $\beta = 0.01$, $\alpha = 1$. See Supplemental Material [42] for the associated animations.

Examples of such grain-boundary nucleation processes in fcc nanopolycrystals are shown in Figs. 5(a)–5(d) (see Supplemental Material [42] for the associated animation). This system has the same model parameters as those of Figs. 3 and 4, and the grain structures were formed using Voronoi tessellation. Tensile strain ϵ_{zz} was then applied at a constant rate under constant volume conditions, such that $\epsilon_{xx} = \epsilon_{yy} = (\epsilon_{zz} + 1)^{-1/2} - 1$. Shear strain ϵ_{zy} was found to produce similar results. As a point of reference, the simulation shown, which contains $\sim 1.15 \times 10^6$ atoms or density peaks, required 57 hours of wall-clock time to execute 2.4×10^4 time steps (or ~ 3 ms estimated duration for Cu at 1063 °C) using 48 CPU cores. A direct comparison with LAMMPS benchmark data for Cu with an EAM potential [53] indicates that the same computation of $\sim 1.15 \times 10^6$ atoms for 3 ms on 48 CPU cores would require $\sim 1.25 \times 10^8$ h of wall-clock time, more than six orders of magnitude greater than the PFC time.

Examples of the spontaneous nucleation of complete dissociated $a/2\langle 110\rangle$ dislocations are highlighted with green arrows in Fig. 5. These half-loops traverse the grain and are eventually absorbed into the opposite grain boundary as no fixed obstacles are present. Numerous examples of leading partial nucleation and heavy faulting are also apparent. Each grain has four available $\{111\}$ planes in which the partials may glide, resulting in faulting in some or all of these planes within a given grain. The complex interactions of the various partials and stacking faults lead to varying intragrain textures and structures with results very similar to those produced by MD simulations and consistent with experimental observations [54,55].

The stress-strain curves shown in Fig. 5(e) also confirm this qualitative agreement. Stresses $\sigma_{\rm ij}$ were periodically quantified by measuring the rate of change in average free energy of an instantaneous $n(\vec{r})$ configuration as the appropriate deformation is statically applied. For example, σ_{zz} was measured by varying the grid spacing in the z direction and quantifying $\sigma_{zz} = \delta \bar{F}/\delta\epsilon_{zz}$ in the small strain limit every 10 time steps. Upper and lower yield points are observed for fcc systems with both yield stresses decreasing with decreasing rate, as observed in MD studies [54]. The upper yield point is associated with initiation of plastic flow/dislocation nucleation within the initial clean grains, while the lower yield point is associated with steady-state dislocation and grain-boundary driven plasticity within the resulting dislocated systems. Larger grain sizes produce higher yield points, indicating that these systems are in the reverse Hall-Petch regime [56]. This dominance of dislocation nucleation, glide, and annihilation, and a lack of visible pileups suggests that this reverse Hall-Petch behavior is associated with an absence of pileup-induced hardening at these small grain sizes. Other mechanisms such as grain-boundary sliding and dislocation source starvation may contribute to this behavior as well, but we have not quantified the contributions of such effects. We only note that they are visually less evident than the described dislocation activity.

Analogous simulations of bcc polycrystals produced the results shown in Fig. 5(f) (see Supplemental Material [42] for the associated animation). A simpler yielding behavior is observed in this case, as the bcc nanopolycrystals within this parameter range deform plastically via grain-boundary migration. Very little dislocation nucleation occurs, leaving essentially a network of sliding and creeping grain boundaries. Grain-boundary mechanisms therefore appear to be entirely responsible for the inverse Hall-Petch behavior in these systems. Such behavior is consistent with intermediate- and high-temperature experiments on nanopolycrystalline bcc metals in which grain-boundary mechanisms are found to dominate plasticity [55]. The greater dependence of bcc stress-strain behavior on strain rate also indicates a larger diffusive creep component than in fcc. This is in agreement with general observations of higher creep rates in bcc materials, an effect ascribed to the higher self-diffusivity of non-close-packed structures [57]. These simulations of fcc and bcc polycrystals demonstrate that the qualitative features of conservative dislocation emission from grain boundaries and of overall stress-strain response in elastic and plastic regimes can be well captured by PFC models.

V. BARDEEN-HERRING–TYPE CLIMB SOURCES

Climb-mediated or Bardeen-Herring–type sources can become active at high temperatures or following rapid quenches when the excess vacancy concentration is large. The basic principles are in many ways analogous to those of Frank-Read sources, except that the dislocation motion is mediated by vacancy diffusion rather than by glide. Nonetheless, such sources are not as well understood as Frank-Read sources, at least partly because they are not easily modeled at the atomistic level using conventional approaches, and because mesoscale models must account for the often complex nature of vacancy diffusion around dislocation cores and among other heterogeneous strain fields. We show here that PFC simulations permit the study of such sources with atomistic resolution, and reveal a range of complex nucleation behaviors caused by nontrivial interactions between interface structure, strain orientation, and dislocation energetics.

A. Critical strain for loop nucleation

The specific phenomenon considered in this section is nucleation of dislocation loops from spherical objects such as precipitates, inclusions, or voids in bcc crystals under uniaxial tension or compression ϵ_{ii}. The case of loop nucleation and coherency loss at precipitates has been studied in early theoretical and experimental work [58–61], as precipitate coherency can have a significant impact on the mechanical properties of metal alloys. Concentric dislocation loops centered on precipitates or impurities have also been observed in various metals [62–66]. These may be formed by Bardeen-Herring–type mechanisms similar to those described here. To our knowledge, this problem has not been examined via numerical simulations nor at the atomistic level due to the long, diffusive time scales involved.

As strain is applied to a system containing a spherical precipitate, the free energy eventually becomes higher than that of the same system with a dislocation loop that is able to grow and relieve strain energy. An energy barrier for the nucleation of such a loop will generally exist such that its appearance in a dynamic simulation may be delayed to higher strains. Nonetheless, a loop eventually appears at the sphere-matrix interface, and when the applied strain is purely uniaxial, the nucleation and growth of the loop is largely mediated by climb. Other strain types can lead to different, relatively well-characterized conservative loop formation processes such as prismatic punching [67–69].

In a linear elastic isotropic continuum, the critical strain ϵ_{ii}^* at which loop nucleation becomes favorable is approximately

$$\epsilon_{ii}^* = \frac{b}{8\pi(1-\nu)\left(\frac{B_S}{B_M}-1\right)R_0}\left[\ln\frac{8R_0}{b} + \frac{2\nu-1}{4(1-\nu)}\right], \qquad (7)$$

where b is the magnitude of the dislocation Burgers vector, ν is the Poisson's ratio of the matrix, B_S and B_M are the bulk moduli of the sphere and matrix phases, respectively, and R_0 is the sphere radius [58,61]. We note that anisotropy may play a role in the bcc system studied here.

Homogeneous spherical inclusions were introduced into the present simulations by adding a uniform penalty function over some predefined spherical volume in the center of a simulation cell with initially perfect bcc crystal structure (see Fig. 7). The resulting spherical body has a larger elastic modulus than that of the bulk crystal, but since $n(\vec{r})$ within the sphere is uniform rather than periodic, the issue of coherent versus incoherent interface structure is not relevant. After the system was equilibrated, uniaxial strain ϵ_{ii} was applied at a constant rate by uniformly increasing or decreasing the numerical grid spacing along one axis of the periodic simulation cell by a small amount at every time step.

Equations (1), (3), and (4) were employed in all simulations discussed in this section. Parameter values used were $w = 1.4$, $u = 1$, $n_0 = 0$, $\alpha_1 = 1$, $\sigma = 0.1$, $\rho_1 = 1$, and $\beta_1 = 8$. Other simulation details are given here [70]. Following the procedure used for fcc simulations, if we match the numerically measured bcc vacancy diffusion constant $D_v \simeq 1.5a^2/t$ to that of vanadium at 1842 °C ($D_v \simeq 1.36 \times 10^{-13}$ m^2/s, $a \simeq 0.302$ nm), then the time unit t is found to correspond to $\sim$1 μs. The range of shear rates used in bcc simulations then converts to $\sim$20/s–2500/s, values again roughly four to six orders of magnitude lower than those of typical and comparable MD simulations.

Compiled results for the critical nucleation strain ϵ_{ii}^* at all sphere sizes and strain orientations are shown in Fig. 6. The agreement between the low strain rate results and the static energy minimization results indicates that any rate dependence is minimal at the slower rate considered. The general trend is a decrease in ϵ_{ii}^* as R_0 increases. The form of the decrease is well described by Eq. (7) after an additional constant strain $\epsilon_{ii}^{\min}$ is added to the right-hand side. This constant is discussed further in the following paragraph. The adjustable parameters in the fits shown are therefore $\epsilon_{ii}^{\min}$ and B_S, as there are some ambiguities in the effective value of the bulk modulus of the sphere as modeled. Nonetheless, the fits are quite good for $B_S/B_M \simeq 4$, which seems to be a reasonable estimate of the ratio produced by our simulations.

It is not conclusive whether ϵ_{ii}^* will continue to slowly decrease as R_0 becomes very large or whether it levels off to some minimum value. Our expectation is that ϵ_{ii}^* will plateau in the PFC simulations due to finite-size effects as well as the existence of a threshold Eckhaus-type strain for activation of the wavelength selection or climb "instability" [71]. Both of these effects are driven by lattice periodicity. An integer number of unit cells must fit into the simulation box, such that the energy of a perfect crystal will not be reduced by the addition or removal of a plane of atoms or density peaks until $\epsilon_{ii} > 1/(2N_i)$, where N_i is the number of unit cells in the i direction. Furthermore, there will be an energy barrier for this

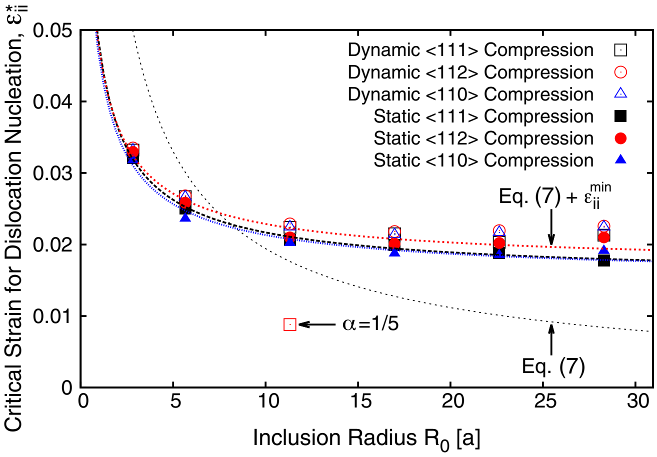

FIG. 6. (Color online) Critical strain ϵ_{ii}^* for Bardeen-Herring climb source activation vs sphere radius R_0. The points represent simulation data at different effective strain rates, and the lines are predictions of the theory of Brown *et al.* [58], without and with a finite minimum critical strain. The fits employ fixed parameters $b = 1/\sqrt{2}$ and $\nu = \frac{1}{3}$, and adjustable parameters $\epsilon_{ii}^{\min}$ and B_S/B_M, which are in all cases close to 0.016 and 4, respectively.

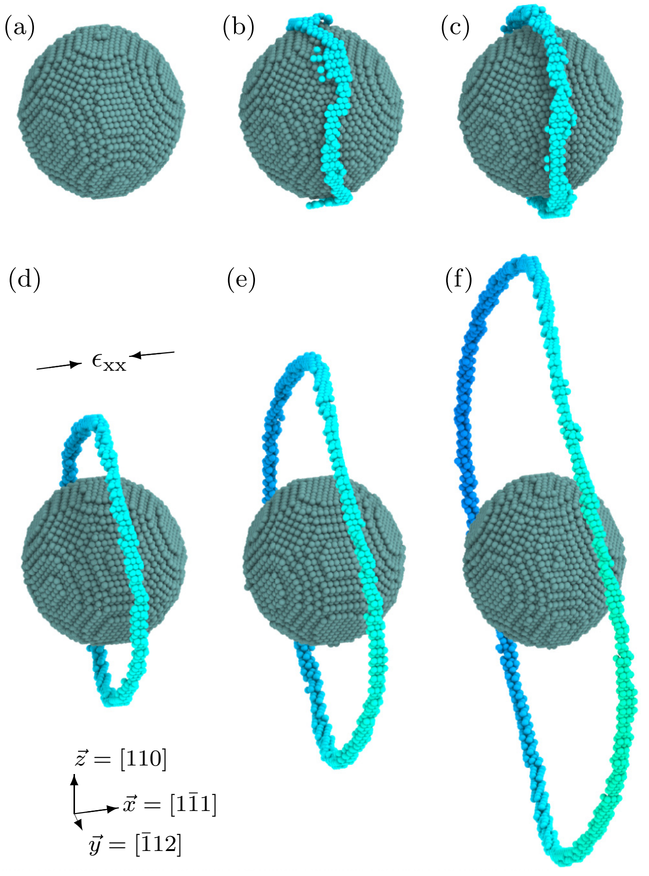

FIG. 7. (Color online) Operation of a Bardeen-Herring–type spherical climb source with $R_0 = 11.3a$ in a bcc crystal under uniaxial compression ϵ_{xx}. Time evolution shown at (a) $t = 110$, (b) $t = 126$, (c) $t = 135$, (d) $t = 145$, (e) $t = 160$, and (f) $t = 180$. Only density peaks with irregular coordination (interface and dislocation core sites) are displayed. Those at the sphere-matrix interface are shown in gray (dark), those inside the dislocation core are shown in blue-green (light) depending on position along the y axis. See Supplemental Material [42] for the associated animation.

removal process associated with an Eckhaus-type instability strain, which quantifies the strain at which this barrier goes to zero [71]. Thus, without thermal fluctuations we expect to observe $\epsilon_{ii}^* > 1/(2N_i) \simeq 0.009$ for the system size used in this study. As the elastic moduli become large, $\epsilon_{ii}^* \rightarrow 1/(2N_i)$ since the perfect crystal Eckhaus strain is roughly proportional to α_i. The single data point at $\alpha_1 = \frac{1}{5}$, $R_0 = 15.8b$ is consistent with this expectation.

B. Loop geometry and evolution

The critical strain for nucleation is therefore in general agreement with continuum elastic predictions, but it is worthwhile to examine the nucleation and growth process in greater detail. A typical result from the dynamic simulations is shown in Fig. 7 (see Supplemental Material [42] for the associated animation). The sphere radius in this case is $R_0 = 11.3a$, and the strain is compressive along the x axis ϵ_{xx}. A loop first begins to form at the sphere-matrix interface with a slightly serpentine shape due to the variations in local line energy around the surface of the sphere. Essentially, the nature in which the spherical surface intersects the various crystallographic planes of the matrix creates a quasi-2D energy landscape on the spherical surface which the dislocation loop must navigate to minimize its total energy with the constraint of fixed total Burgers vector. Certain planes and line directions will be preferred over others. This effect involves not only crystallographically dependent dislocation energies, but also atomic-level core structure effects as well as elastic anisotropy, which together are beyond the scope of continuum elastic theories. The impact on initial loop shape tends to be small for small R_0 but increases considerably for larger R_0 values, as will be shown.

The initial loop nucleation and its subsequent growth both require vacancy diffusion to or away from the surface of the sphere. In the PFC approach, this process is mediated by local diffusive modes of the density wave amplitudes. After the loop detaches from the sphere, its shape continues to evolve as the effective local energy landscape changes with loop radius. Nonplanar, noncircular shapes are common as the competition between minimum static energy and lowest-energy pathway to continued growth can be delicate and nontrivial. This is somewhat analogous to the cross slip of dissociated screw dislocations, during which local segments must constrict at large energy cost to permit cross slip into the next local energy minimum. Any instantaneous configuration may not be the lowest-energy static configuration for the given loop radius, but it should facilitate evolution toward an even lower-energy state with larger radius.

A more complex loop nucleation process is shown in Fig. 8 (see Supplemental Material [42] for the associated animation). The only difference from Fig. 7 is the increased sphere size of $R_0 = 28.3a$. The result is a much more pronounced serpentine shape due to the larger areas on the surface of the sphere that nearly coincide with low-energy lattice planes of the matrix. Within the (110) plane, for example, the preferred line direction for the nucleated $a/2[1\bar{1}1]$ dislocation is along the nearest $\langle 001 \rangle$ vector rather than the $[\bar{1}12]$ vector normal to the strain axis. The dislocation therefore forms with mixed edge-screw character along the [001] direction within the uppermost (110) plane, for example, taking the loop locally out of alignment with the strain-normal $(1\bar{1}1)$ plane. The line must then wind back toward the strain-normal plane in the areas where it curves out of the top and bottom (110) planes.

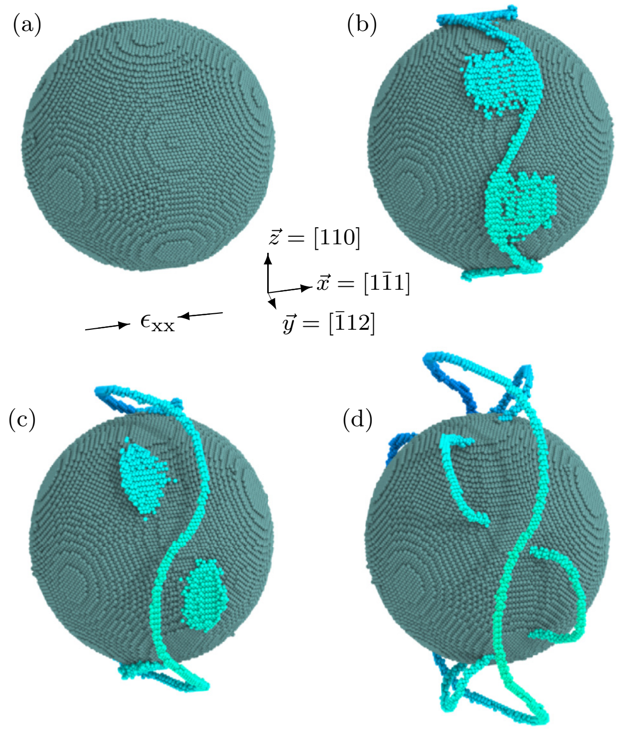

FIG. 8. (Color online) Operation of a Bardeen-Herring–type spherical climb source with $R_0 = 28.3a$ in a bcc crystal under uniaxial compression ϵ_{xx}. Time evolution shown at (a) $t = 110$, (b) $t = 138$, (c) $t = 150$, and (d) $t = 162$. Only density peaks with irregular coordination (interface and dislocation core sites) are displayed. Those at the sphere-matrix interface are shown in gray (dark), those inside the dislocation core are shown in blue-green (light) depending on position along the y axis. See Supplemental Material [42] for the associated animation.

The same arguments hold as the line crosses through the other intersecting {110} planes. The $a/2[1\bar{1}1](011)$ segments, for example, prefer alignment with the $[\bar{1}00]$ direction. The $a/2[1\bar{1}1](\bar{1}12)$ segments on the other hand prefer alignment with the [110] direction (pure edge character). Thus, a serpentine winding pattern is produced as a result of the dynamic competition between loop energy minimization, which tends to promote a certain degree of winding, and strain relief maximization, which tends to suppress winding in favor of maximizing the outward growth (climb) velocity.

Detachment and growth away from the sphere occur first in regions that do not align with any low-energy dislocation slip planes. Segments in low-energy {110} planes are observed to detach last, as these have the lowest local energy and the highest barrier for out-of-plane motion. Terrace sites at the edges of faceted low-energy planes in particular appear to have the maximum detachment barrier. The extra half-loops protruding from the sphere in Fig. 8 are a dynamic effect that disappears at low applied strain rates.

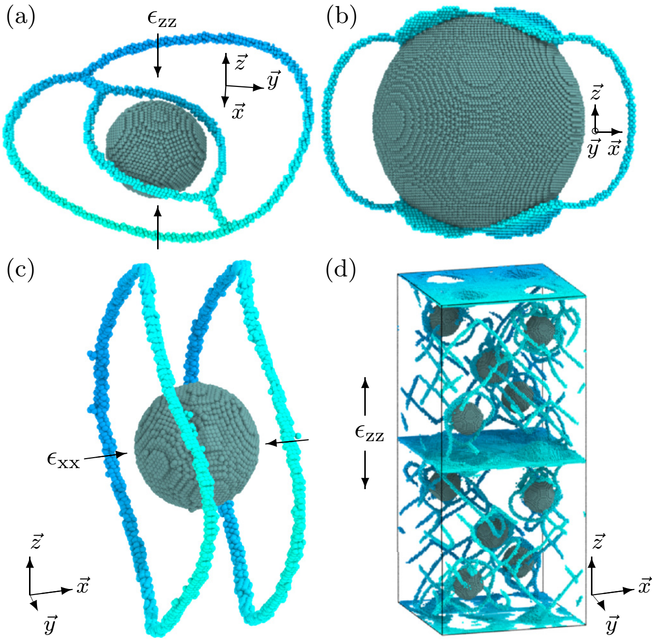

FIG. 9. (Color online) Examples of various other Bardeen-Herring–type climb sources in bcc crystals. (a) Linked, concentric, biplanar loop pairs under ϵ_{zz} with $R_0 = 11.3a$. (b) Offset nonconcentric loop pairs under ϵ_{yy} with $R_0 = 28.3a$. (c) Offset concentric loop pairs under ϵ_{xx} with $R_0 = 9a$ and $\alpha = 2$. (d) Dislocation network/tangle formation from an array of 10 sources with $R_0 = 9a$ in a bicrystal under constant volume tension ϵ_{zz}. Only density peaks with irregular coordination (interface and dislocation core sites) are shown. Those at the sphere-matrix interface are shown in gray (dark), those inside the dislocation core are shown in blue-green (light) depending on position along the out-of-plane axis. See Supplemental Material [42] for the associated animations.

Other variations of climb-mediated loop nucleation processes are shown in Fig. 9 (see Supplemental Material [42] for the associated animations). Uniaxial strain along a $\langle 110\rangle$ direction produces two disjointed $a/2\langle 111\rangle$ half-loops that grow symmetrically at a 12.5° angle to the strain-normal (110) plane [Fig. 9(a)]. An $a\langle 100\rangle$ edge line segment appears at the intersection of these half-loops, and can link to a second, concentric inner pair of half-loops that allows complete detachment from the sphere. Uniaxial strain along a $\langle 112\rangle$ direction produces two separate $a/2\langle 111\rangle$ edge dislocation half-loops, as displayed in Fig. 9(b). These half-loops climb until their terminal ends meet and merge into a single, nearly circular loop. Dual loop nucleation as shown in Fig. 9(c) is also possible for certain R_0, elastic moduli, and strain rates. Finally, arrays of spheres simultaneously nucleate complex networks of dislocation lines via mixed climb-glide processes. Effects from dislocation-dislocation, dislocation-grain boundary, and dislocation-inclusion interactions, for example, are naturally incorporated into the evolution of such networks in PFC simulations.

VI. DISLOCATION-SFT INTERACTIONS

Impediments to dislocation motion, including other dislocations, planar faults, and 3D obstacles, play a central role in the mechanical response and work-hardening properties of metals. The dominant irradiation-induced defect in fcc materials is the SFT, and dislocation-SFT interactions are therefore believed to largely control the mechanical response of fcc materials in nuclear applications [72]. Such interactions have been widely studied in MD (and DDD) simulations [49,72,73] providing for our purposes a potentially useful body of benchmark results with which PFC simulations can be compared. A few selected results are presented in this section.

SFTs were formed in the present simulations via the Silcox-Hirsch mechanism [74]. A triangular Frank loop is initiated on a $\{111\}$ plane, after which it spontaneously relaxes into the local energy minimum corresponding to a perfect SFT with base prescribed by the initial Frank loop (see Supplemental Material [42] for the associated animation). Dissociated $a/2\langle 110\rangle$ edge or screw dislocations were equilibrated some lateral distance away from the SFT and some vertical distance relative to the SFT base. Shear strain ϵ_{zx} was then applied at a constant rate to cause the dislocation to glide toward and through the SFT (see Fig. 10).

Only two cases will be reported here, given in the notation of Ref. [49] as (ED/Down,4/13,0.0001/t) and (SD/Edge,4/13,0.0001/t). In the first case, this notation indicates that an edge dislocation (ED) intersects a SFT with apex oriented in the $[\bar{1}1\bar{1}]$ direction (Down), at the fourth $\{111\}$ plane from the base of the SFT which is 13 $\{111\}$ planes tall (4/13), and with shear rate 0.0001/t. The second case is the same except that it considers a screw dislocation (SD) intersecting a SFT with one edge oriented along the SD line direction (Edge). Additional simulations details are given here [75]. Results from the (ED/Down,4/13,0.0001/t) simulation are shown in Fig. 10. The accompanying animation, along with that of the SFT-screw dislocation interaction, can be found in the Supplemental Material [42].

The general sequence of events includes dislocation pinning at SFT Lomer-Cottrell stair rod junctions, bow out of the gliding dislocation line between the image SFTs, Orowan looping of the SFT by the leading partial, and damage of the SFT after the trailing partial has passed through. The pinning and bow-out effects are of course expected. The Orowan loop created by the leading partial is also consistent with MD simulations of individual Shockley partial-SFT interactions [73]. In the present simulations, the trailing partial eventually shears the SFT as well, clearing the Orowan loop and leaving either one or two ledges on the SFT faces. The ledge structures appear to be consistent with those observed in MD [49]. The height of the SFT apex above is also reduced by one $\{111\}$ interplanar distance in the ED case.

We have not yet observed other possible outcomes reported in MD simulations, such as partial SFT absorption and jog formation, but we have considered only a very small subset of the conditions examined via MD. We therefore argue that these results provide partial but strong qualitative evidence that PFC simulations can correctly reproduce complex defect phenomena of this type.

VII. CONCLUSIONS

Basic dislocation properties in fcc and bcc crystals have been examined in the context of phase field crystal models, and

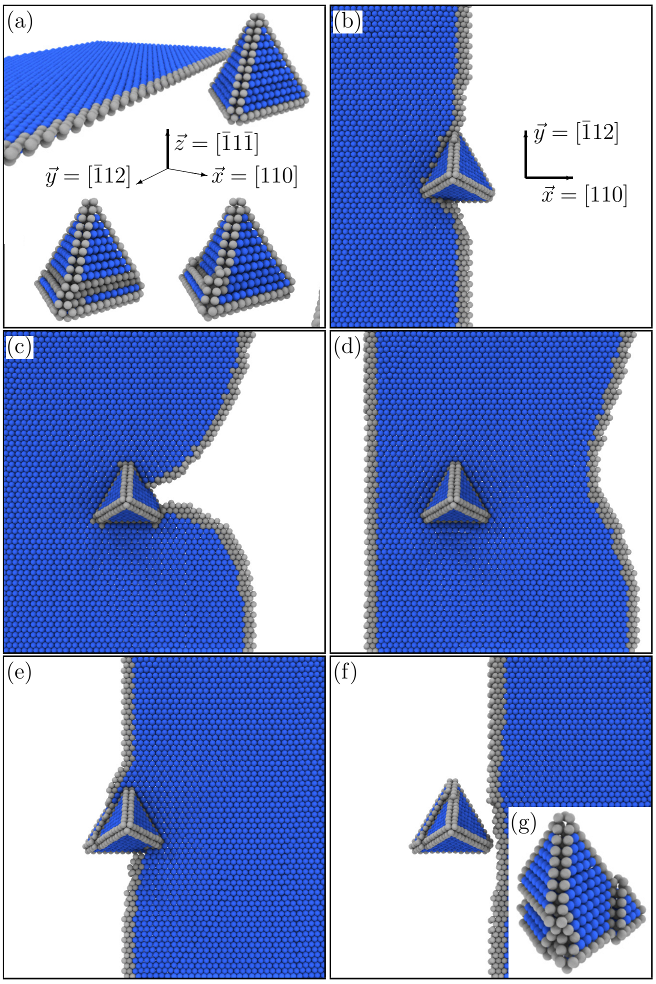

FIG. 10. (Color online) Interaction between a SFT and a gliding dissociated edge dislocation in a fcc crystal, (ED/Down,4/13,0.0001/t). Perspective views of the SFT and dislocation are shown in (a). The upper image shows both at $t = 10\,100$, while the lower left and right images show the SFT at $t = 15\,800$ and $20\,100$, respectively. Only the leading partial has passed the SFT at $t = 15\,800$, both partials have passed by $t = 20\,100$. xy-plane views are shown in (b), (c), (d), (e), and (f) at $t = 12\,100$, $15\,100$, $16\,600$, $18\,600$, and $19\,600$, respectively. (g) The damaged SFT following the (SD/Edge,4/13,0.0001/t) interaction. Density peaks with hcp coordination (stacking faults) are shown in blue (dark gray), those with irregular coordination (dislocation cores) are shown in gray (light gray). See Supplemental Material [42] for the associated animations.

extended into simulations of conservative and nonconservative dislocation creation mechanisms and obstacle flow processes. Core structures of dissociated $a/2\langle 110\rangle$ fcc dislocations and $a/2\langle 111\rangle$ bcc dislocations have now been reproduced in PFC with sufficient accuracy to capture many aspects of plastic flow that derive from such structures. These include the known anisotropy in bcc screw-edge glide mobility as well as the effect of fcc dissociation width on cross-slip and climb barriers. Classical Frank-Read–type sources have been simulated with such models, and a new mechanism by which dislocation lines or superjogs under strain can segment onto multiple glide planes, converting local monopole or dipole sources into multipole sources, has been identified. Stacking fault tetrahedra under high strain have also been shown to reconstruct and emit dislocations via a Frank-Read–type mechanism. Basic features of 3D polycrystal plasticity and dislocation emission from grain boundaries have also been examined and shown to be consistent with MD simulation results.

Nonconservative dislocation creation mechanisms associated with spherical precipitates, inclusions, or voids have been studied using atomistic simulations. Results for the critical strain to nucleate a loop from a spherical body are in agreement with predictions of continuum elastic theory after accounting for finite-size effects and moduli-dependent climb barriers present in our simulations. A range of complex nucleation behaviors caused by nontrivial interactions between interface structure, strain orientation, and dislocation energetics have been revealed. Observed loop geometries have been rationalized for a few select cases, but the results in general highlight the sometimes unexpected complexity that can emerge when atomistic effects associated with crystal structure, dislocation cores, and climb dynamics are simultaneously considered.

The Silcox-Hirsch SFT formation mechanism has also been reproduced, as well as qualitative features of SFT-dislocation interactions observed in MD and DDD simulations. Such processes will require further study to gain a fuller understanding of the similarities and differences between PFC and other atomistic simulation methods. But, there appears to be promise in the possibility of simulating features of obstacle flow involving, for example, climb bypass mechanisms that can not be accessed with other conventional methods.

In a wider sense, it is hoped that these results convey the potential of the PFC approach as applied to solid-state materials phenomena in three dimensions. This type of description unifies conservative and nonconservative plastic flow mechanisms with atomistic resolution, enabling the study of complex high-temperature diffusive evolution processes in the nanoscale-size regime. Many such processes are inaccessible to conventional atomistic approaches. Applications to pure or multicomponent systems and phenomena such as creep, recovery, recrystallization, grain growth, structural phase transformations, and strain-hardening have already been reported or are currently underway. The additional, coupled effect of solute diffusion in alloy materials is naturally incorporated into PFC-type descriptions. Issues that we believe require further development or should be kept in mind include choice of ensemble, control of stress-strain-volume relations, quantification of vacancy concentration, and its connection to climb rates.

ACKNOWLEDGMENTS

This work has been supported by the Natural Science and Engineering Research Council of Canada (NSERC), and supercomputing resources have been provided by CLUMEQ/Compute Canada. The atomic visualization and analysis packages OVITO [76] and the Dislocation Extraction Algorithm (DXA) [77] were used in this work.

[1] V. Bulatov and W. Cai, *Computer Simulations of Dislocations*, Osmm Series (Oxford University Press, Oxford, 2006).

[2] V. Yamakov, D. Wolf, S. R. Phillpot, A. K. Mukherjee, and H. Gleiter, Nat. Mater. **1**, 45 (2002).

[3] R. J. Amodeo and N. M. Ghoniem, Phys. Rev. B **41**, 6958 (1990).

[4] S. Groh and H. M. Zbib, J. Eng. Mater. Technol. **131**, 041209 (2009).

[5] D. Rodney, Y. L. Bouar, and A. Finel, Acta Mater. **51**, 17 (2003).

[6] Y. Wang and J. Li, Acta Mater. **58**, 1212 (2010).

[7] D. Raabe, Comput. Mater. Sci. **11**, 1 (1998).

[8] D. Mordehai, E. Clouet, M. Fivel, and M. Verdier, Philos. Mag. **88**, 899 (2008).

[9] Y. Gao, Z. Zhuang, Z. Liu, X. You, X. Zhao, and Z. Zhang, Int. J. Plast. **27**, 1055 (2011).

[10] C. Ayas, J. A. W. van Dommelen, and V. S. Deshpande, J. Mech. Phys. Solids **62**, 113 (2014).

[11] Y. Li, S. Hu, C. H. Henager, Jr., H. Deng, F. Gao, X. Sun, and M. A. Khaleel, J. Nucl. Mater. **427**, 259 (2012).

[12] P.-A. Geslin, B. Appolaire, and A. Finel, Appl. Phys. Lett. **104**, 011903 (2014).

[13] K. R. Elder, M. Katakowski, M. Haataja, and M. Grant, Phys. Rev. Lett. **88**, 245701 (2002).

[14] K. R. Elder and M. Grant, Phys. Rev. E **70**, 051605 (2004).

[15] K. R. Elder, N. Provatas, J. Berry, P. Stefanovic, and M. Grant, Phys. Rev. B **75**, 064107 (2007).

[16] N. Goldenfeld, B. P. Athreya, and J. A. Dantzig, Phys. Rev. E **72**, 020601 (2005).

[17] B. P. Athreya, N. Goldenfeld, J. A. Dantzig, M. Greenwood, and N. Provatas, Phys. Rev. E **76**, 056706 (2007).

[18] D. Yeon, Z. Huang, K. R. Elder, and K. Thornton, Philos. Mag. **90**, 237 (2010).

[19] Z.-F. Huang, K. R. Elder, and N. Provatas, Phys. Rev. E **82**, 021605 (2010).

[20] R. Spatschek and A. Karma, Phys. Rev. B **81**, 214201 (2010).

[21] N. Ofori-Opoku, J. Stolle, Z.-F. Huang, and N. Provatas, Phys. Rev. B **88**, 104106 (2013).

[22] M. Greenwood, N. Provatas, and J. Rottler, Phys. Rev. Lett. **105**, 045702 (2010).

[23] M. Greenwood, J. Rottler, and N. Provatas, Phys. Rev. E **83**, 031601 (2011).

[24] M. Greenwood, N. Ofori-Opoku, J. Rottler, and N. Provatas, Phys. Rev. B **84**, 064104 (2011).

[25] J. Berry, N. Provatas, J. Rottler, and C. W. Sinclair, Phys. Rev. B **86**, 224112 (2012).

[26] N. Ofori-Opoku, V. Fallah, M. Greenwood, S. Esmaeili, and N. Provatas, Phys. Rev. B **87**, 134105 (2013).

[27] J. Berry, M. Grant, and K. R. Elder, Phys. Rev. E **73**, 031609 (2006).

[28] P. Stefanovic, M. Haataja, and N. Provatas, Phys. Rev. Lett. **96**, 225504 (2006).

[29] P. Stefanovic, M. Haataja, and N. Provatas, Phys. Rev. E **80**, 046107 (2009).

[30] T. Hirouchi, T. Takaki, and Y. Tomita, Comp. Mater. Sci. **44**, 1192 (2009).

[31] P. Y. Chan, G. Tsekenis, J. Dantzig, K. A. Dahmen, and N. Goldenfeld, Phys. Rev. Lett. **105**, 015502 (2010).

[32] A. Jaatinen, C. V. Achim, K. R. Elder, and T. Ala-Nissila, Phys. Rev. E **80**, 031602 (2009).

[33] R. Backofen, A. Voigt, and T. Witkowski, Phys. Rev. E **81**, 025701(R) (2010).

[34] A. Jaatinen, C. V. Achim, K. R. Elder, and T. Ala-Nissila, Techn. Mech. **30**, 169 (2010).

[35] J. Berry, K. R. Elder, and M. Grant, Phys. Rev. B **77**, 224114 (2008).

[36] J. Mellenthin, A. Karma, and M. Plapp, Phys. Rev. B **78**, 184110 (2008).

[37] D. L. Olmsted, D. Buta, A. Adland, S. M. Foiles, M. Asta, and A. Karma, Phys. Rev. Lett. **106**, 046101 (2011).

[38] E. J. Schwalbach, J. A. Warren, K.-A. Wu, and P. W. Voorhees, Phys. Rev. E **88**, 023306 (2013).

[39] L. Kubin, B. Devincre, and M. Tang, J. Comput.-Aided Mater. Des. **5**, 31 (1998).

[40] See R. Gröger and V. Vitek, Philos. Mag. **89**, 3163 (2009) for an overview of such studies. We have not yet observed the other primary core structure (degenerate polarized) predicted by some MD potentials, but the resulting glide mobility has been found to be nearly the same for both core types.

[41] V. Vitek, R. C. Perrin, and D. K. Bowen, Philos. Mag. **21**, 1049 (1970). The map shows atomic core positions in a projection normal to the [111] dislocation line direction. Circles represent atoms within one pitch of the screw, and shading indicates which of the three successive (111) planes the atomic site belongs to. The arrows quantify the local screw component of the Burgers vector, which is the relative out-of-plane displacement between neighboring atoms. The magnitude of the displacement is proportional to the length of the arrow, which is scaled such that a displacement of $b/3$ would produce an arrow spanning exactly the atomic separation. Arrows in such plots are typically centered between lattice positions, but here instead originate at the lattice position opposite the arrow direction.

[42] See Supplemental Material at http://link.aps.org/supplemental/10.1103/PhysRevB.89.214117 for animations of (i) fcc jog-mediated dislocation climb (S1, S2), (ii) fcc screw dislocation cross slip (S3, S4), (iii) Frank-Read–type fcc dislocation creation mechanisms (S5–S7), (iv) fcc and bcc polycrystal deformation (S8, S9), (v) Bardeen-Herring–type bcc climb-mediated dislocation creation mechanisms (S10–S15), (vi) fcc SFT formation (S16), and (vii) fcc SFT-dislocation interactions (S17, S18).

[43] M. Kabir, T. T. Lau, D. Rodney, S. Yip, and K. J. Van Vliet, Phys. Rev. Lett. **105**, 095501 (2010).

[44] M. de Koning, W. Cai, and V. V. Bulatov, Phys. Rev. Lett. **91**, 025503 (2003).

[45] J. P. Hirth and J. Lothe, *Theory of Dislocations*, 2nd ed. (Wiley, New York, 1982).

[46] L. Kubin, *Dislocations, Mesoscale Simulations and Plastic Flow* (Oxford University Press, Oxford, UK, 2013).

[47] R. Madec, P. Veyssière, and G. Saada, Philos. Mag. **93**, 222 (2013).

[48] Numerical grid spacing $\Delta x = a/(6\sqrt{6})$, time step $\Delta t = 0.1$, and penalty parameters $L_\ell = 20\Delta x$, $M_\ell = 1$, $L_P = 24\Delta x$, $M_P = 0.05$ were also used, where $a = 1.8537$. In Fig. 3, system dimensions $N_x = 68\sqrt{6}a$, $N_y = 117\sqrt{2}a$, and $N_z = 37a/\sqrt{3}$ were used ($\sim 2.5 \times 10^6$ atoms or density peaks), along with loop dimensions $L_x = 10\sqrt{6}a$, $L_z = 4\sqrt{3}a$, and shear rate $\dot{\epsilon}_{\mathrm{zy}} = 0.000\,235/t$. In Fig. 4, system dimensions $N_x = 68\sqrt{6}a$, $N_y = 80\sqrt{2}a$, and $N_z = 55a/\sqrt{3}$ were used ($\sim 2.4 \times 10^6$ atoms or density peaks), along with loop dimensions $L_x = 5\sqrt{6}a$, $L_z = 9\sqrt{3}a$, and shear rate $\dot{\epsilon}_{\mathrm{zy}} = 0.000\,235/t$.

[49] Y. N. Osetsky, D. Rodney, and D. J. Bacon, Philos. Mag. **86**, 2295 (2006).

[50] C. R. Weinberger and W. Cai, Scr. Mater. **64**, 529 (2011).

[51] C. R. Weinberger and G. J. Tucker, Modell. Simul. Mater. Sci. Eng. **20**, 075001 (2012).

[52] D. Rodney and R. Phillips, Phys. Rev. Lett. **82**, 1704 (1999).

[53] http://lammps.sandia.gov/bench/eam_cluster.html.

[54] H. V. Swygenhoven and P. Derlet, in *Dislocations in Solids*, edited by J. Hirth (Elsevier, Amsterdam, 2008), Vol. 14, pp. 1–42.

[55] G. Saada and G. Dirras, in *Dislocations in Solids*, edited by J. Hirth and L. Kubin (Elsevier, Amsterdam, 2009), Vol. 15, pp. 199–248.

[56] M. A. Meyers, A. Mishra, and D. J. Benson, Prog. Mater. Sci. **51**, 427 (2006).

[57] H. Frost and F. Ashby, *Deformation-Mechanism Maps: The Plasticity and Creep of Metals and Ceramics* (Pergamon, New York, 1982).

[58] L. M. Brown, G. R. Woolhouse, and U. Valdrè, Philos. Mag. **17**, 781 (1968).

[59] G. C. Weatherly, Philos. Mag. **17**, 791 (1968).

[60] M. F. Ashby, S. H. Gelles, and L. E. Tanner, Philos. Mag. **19**, 757 (1969).

[61] L. M. Brown and G. R. Woolhouse, Philos. Mag. **21**, 329 (1970).

[62] A. Sato, Y. Sugisaki, and T. Mori, Philos. Mag. A **51**, 133 (1985).

[63] K. H. Westmacott, R. S. Barnes, and R. E. Smallman, Philos. Mag. **7**, 1585 (1962).

[64] J. Embury and R. Nicholson, Acta Metall. **11**, 347 (1963).

[65] J. W. Edington and D. R. West, J. Appl. Phys. **37**, 3904 (1966).

[66] Y. G. Zhang and I. P. Jones, Radiat. Eff. Defects Solids **108**, 45 (1989).

[67] R. Balluffi, S. Allen, and W. Carter, *Kinetics of Materials* (Wiley, Hoboken, NJ, 2005).

[68] R. E. Rudd, Philos. Mag. **89**, 3133 (2009).

[69] R. Calhoun and A. Mortensen, Acta Mater. **47**, 2357 (1999).

[70] Numerical grid spacing $\Delta x = \sqrt{2}a/16$ and time step $\Delta t = 0.01$ were used, where $a \simeq 0.817$. System dimensions were varied to confirm the absence of large finite-size effects, and results are presented for the case of $N_x = 54\sqrt{3}a$, $N_y = 38\sqrt{6}a$, and $N_z = 66\sqrt{2}a$ ($\sim 1.6 \times 10^6$ atoms or density peaks). Sphere radii $R_0 = 2.83a$, $5.66a$, $11.3a$, $16.97a$, $22.63a$, and $28.28a$ were examined with strain rates of $\dot{\epsilon}_{ii} = 0.0025/t$ and $0.000\,125/t$. The x, y, and z axes of the simulation cell are aligned with the $[1\bar{1}1]$, $[\bar{1}12]$, and $[110]$ directions of the bcc crystal, respectively, and strain was applied separately along each direction. A quasistatic case was considered as well, in which the free energy of a configuration consisting of sphere and dislocation loop with radius R_0 was measured as a function of ϵ_{ii}, without any dynamics. The strain at which the free energy equals that of the undislocated system is taken to be ϵ^*_{ii}.

[71] N. Provatas and K. Elder, *Phase-Field Methods in Materials Science and Engineering* (Wiley-VCH, Weinheim, Germany, 2011).

[72] J. Marian, E. Martínez, H.-J. Lee, and B. D. Wirth, J. Mater. Res. **24**, 3628 (2009).

[73] M. Niewczas and R. Hoagland, Philos. Mag. **89**, 623 (2009).

[74] J. Silcox and P. B. Hirsch, Philos. Mag. **4**, 72 (1959).

[75] All parameters are the same as those of Sec. IV A, except $H_0 = 0$ (low stacking fault energy, wide dissociation). For the ED, system dimensions $N_x = 16\sqrt{6}a$, $N_y = 87.25\sqrt{2}a$, and $N_z = 41\sqrt{3}a$ were used with $\Delta x = a\sqrt{6}/32$. For the SD, system dimensions $N_x = 28\sqrt{2}a$, $N_y = 78\sqrt{6}a$, and $N_z = 40\sqrt{3}a$ were used with $\Delta x = a/(10\sqrt{2})$.

[76] A. Stukowski, Modell. Simul. Mater. Sci. Eng. **18**, 015012 (2010).

[77] A. Stukowski, V. V. Bulatov, and A. Arsenlis, Modell. Simul. Mater. Sci. Eng. **20**, 085007 (2012).